

The application of large format, broadband QWIP arrays to Spatially Modulated Prism Interferometers

Francis M. Reininger

Jet Propulsion Laboratory, 4800 Oak Grove Drive, Pasadena, California 91109
email: fmr@jpl.nasa.gov; tel: 818-354-1299; fax: 818-393-6047

27 July 2000

Abstract

The Spatially Modulated Prism Interferometer (SMPI) is a new type of imaging interferometer that has double the efficiency of conventional interferometers and only a fraction of the mass and volume. Its spectral resolution is independent of wavelength and slit width, an attribute made possible by generating interferograms at a pupil plane. It uses a large format, broadband Quantum Well Infrared Photodetector (QWIP) array to scan the interferograms digitally without moving any optical components. This enables the interferometer to make accurate measurements of target scenes that fluctuate during the scan period. Applications include detecting water sources on Mars, monitoring global warming and ozone depletion on Earth, monitoring pollution in cities, detecting chemical agents on the battlefield, and warning commercial aircraft of volcanic eruptions.

1 Introduction

Ever since Mariner 9 discovered channels and valleys on Mars, scientists have postulated that at one time liquid water flowed across its surface [1]. Though the geological evidence seemed to indicate that the water disappeared from the surface billions of years ago, images taken in 1999 by the Mars Global Surveyor (MGS) spacecraft showed recently formed gullies [2]. The principal investigator for the MGS camera experiment, Michael Malin, has suggested that the gullies “could be a few million years old, but we cannot rule out that some of them are so recent as to have formed yesterday.” This would imply that an aquifer could exist within a few hundred meters of the surface and occasionally supply the gullies with liquid water. Unfortunately the average atmospheric pressure at the surface of Mars is only 5.6 mbar, so the water would immediately boil upon reaching the gullies. This makes it very difficult for an imaging camera to prove the existence of surface water unless it can record a flash flood in real-time.

The Spatially Modulated Prism Interferometer (SMPI) can establish the existence of surface water without capturing an event in progress. It can measure the hydration content of the surrounding debris, which will remain at an elevated level long after the flash flood has subsided. It can also measure the water vapor abundances immediately above the flood sites, which will be significantly higher than the average atmospheric vapor levels. The average water vapor abundance in a column of Martian atmosphere is only 10 - 20 precipital¹ microns (μm), and the expected water vapor abundance in a vapor plume would be several hundred μm . This would make it very easy for the SMPI to detect a plume from a flash flood or a water vapor source.

The importance of using a spectrum to identify a water vapor plume is made apparent in the two Viking Orbiter images shown in figure 1. On the left is an image of a possible water vapor plume that was announced in 1980 by Leonard Martin of the Lowell Observatory [3]. It is one of two images collected by the Viking Orbiter in an interval of 4.5 seconds. The region is just north of Solis Lacus in the southern hemisphere. The image on the right shows a field of dust devils. Though the dust devils were imaged at a much lower resolution, it is apparent that the dust devils and the ‘vapor plume’ have nearly identical visual signatures. One obvious explanation is that the ‘vapor plume’ is a dust devil. However, dust devils tend to rotate, leave

¹A precipital micron is a measure of the water depth in a column of atmosphere if it could be condensed at the surface. The average depth on Earth would be 40 millimeters.

tracks, and exist in groups. All of these characteristics were absent in the two ‘vapor plume’ images, which did not change in the 4.5 second collection interval.

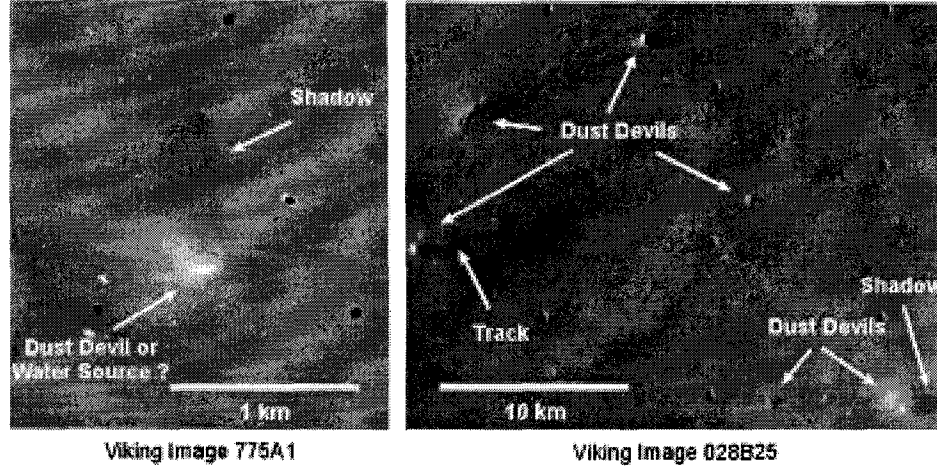


Figure 1: Viking Orbiter images of a possible water vapor source and a field of dust devils.

The ambiguity of a visual signature is eliminated when a spectrum accompanies the image. For example, a dust devil would have a spectral transmission similar to the ‘high dust’ profile shown in figure 2, with a broad absorption feature between 800 and 1300 cm^{-1} . A water vapor plume would have a spectral transmission similar to the ‘low dust’ profile, with narrow absorption features between 1300 and 1600 cm^{-1} . The ‘high dust’ profile depicts a mild dust storm with an infrared optical depth (IROD) of 0.2. The ‘low dust’ profile assumes an IROD of 0.01. Both simulations rely on the dust extinction spectrum used to predict the performance of the Pressure Modulator Infrared Radiometer [4].

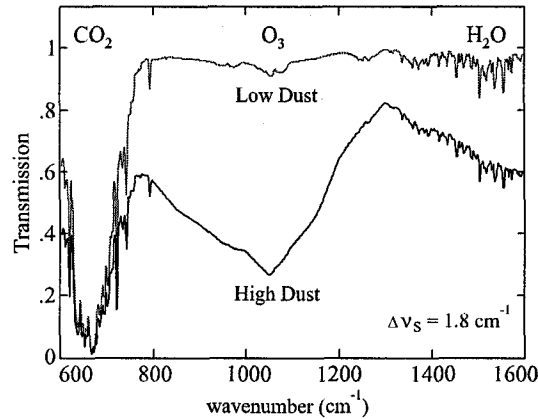


Figure 2: Simulations of the Martian atmosphere under low and high dust conditions (IROD = 0.01 and 0.20). The Mars atmosphere model was developed by Patrick Irwin of Oxford University.

2 Instrument Approach

2.1 Spectral Passband

To detect water vapor sources on Mars, the instrument must operate at wavelengths long enough to minimize the impact of dust scattering, and short enough to prevent diffraction from degrading the spatial resolution. The wavelengths should also be selected to provide the highest signal-to-noise ratio (SNR). The highest signals would be generated when the surface temperature of Mars reaches 270 °K at 12 noon, which places the peak of the Planck radiation function at 10.7 μm . Therefore the ideal spectral bandpass would extend

from 600 - 1600 cm^{-1} and include the CO_2 and H_2O absorption features shown in figure 2. CO_2 is important because it is uniformly mixed from the bottom to the top of the atmosphere, which makes its absorption features ideal for generating atmospheric temperature profiles and humidity maps. It is desirable to measure the water vapor in the 1300 - 1600 cm^{-1} band because it is well separated from any CO_2 bands. A large separation ensures that the tails of the CO_2 lines do not corrupt the water features. In figure 3 is shown a dual broadband QWIP array with exactly the desired spectral coverage. The long wavelength infrared (LWIR) QWIP has been developed, and the middle wavelength infrared (MWIR) QWIP is in development.

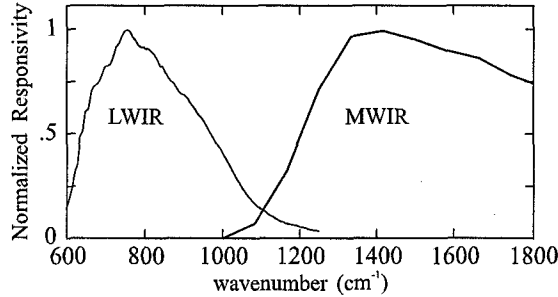


Figure 3: The proposed QWIP spectral profiles for detecting water vapor sources on Mars.

The Spatially Modulated Prism Interferometer is the ideal instrument for the detection of Martian water vapor sources because it can generate spectral images with a very high SNR at a resolution sufficient to detect water vapor sources (if they exist). It would be capable of detecting water vapor to an accuracy of 1 μm under nominal viewing conditions: dust IROD = 0.05 between 10 am and 4 pm. The data would be very reliable because the interferometer generates the interferogram instantaneously without moving any parts. The Michelson interferometer, which must sample the interferogram sequentially in time, would be subject to spectral errors if the scene fluctuates during the sampling period.

2.2 Generating a Spatially Modulated Interference Pattern

The spatial modulation principle is based on Young's double slit experiment [5] in which a beam is widely separated into two mutually coherent halves that interfere in proportion to the path length difference between their wavefronts. The first practical transformation of Young's experiment into a spatially modulated interferometer was accomplished by Stroke and Funkhouser in 1965 [6]. They replaced Young's double slit with a beam-splitter, and they generated the spatially varying optical path difference by tilting the two mirrors in the arms of a Michelson interferometer. The two tilted wavefronts were focused onto a photographic plate to record their resulting interference pattern. An alternative approach is depicted schematically in figure 4 where a lens with a focal length F is positioned at a distance F from the slit plane. A beam-shearing interferometer (not shown) is placed between the slit and the lens to generate two mutually coherent beams. If the two beams are spherical and telecentric² when they enter the lens, then they will depart collimated and converge at a pupil plane. The lens is called a Fourier lens because it performs a spatial Fourier transformation of the image into a pupil. Yoshihara and Kitade in 1967 were the first to generate static fringes at a pupil plane (using a triangle-path Sagnac interferometer) [7]. In 1984 Okamoto, Kawata, and Minami were the first to use a digital detector array to scan a static interferogram [8]. Since that time there have been several groups using two-dimensional arrays to scan the interferogram along one axis and an image along the other axis [9][10][11].

The optical path difference (OPD) measured across the detector array is generated at the reference sphere of the Fourier lens, as indicated by the triangle drawn inside the lens in figure 4. If the input beam is sheared by an amount ΔS , then the variation in OPD across the exit pupil is related to the variation in the angles of the input rays, θ_s , by the law of sines

$$\frac{\delta}{\sin \theta_s} = \frac{\Delta S}{\sin 90^\circ}. \quad (1)$$

At maximum OPD, the maximum ray angle is the 'marginal' ray angle of the lens. The sine of the marginal

²A telecentric beam has its chief ray parallel to the optical axis.

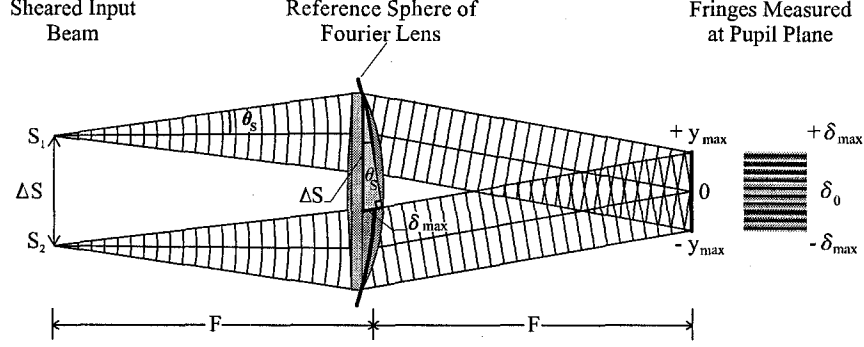


Figure 4: A Fourier lens collimates two mutually coherent, sheared input beams and generates a series of Fizeau fringes at a pupil plane.

ray angle is the numerical aperture, which is equal to $1/2F\#$, so

$$\sin \theta_s = \frac{y_{\max}}{F}. \quad (2)$$

By letting $\delta \rightarrow \delta_{\max}$ in equation 1, and by making the substitution for $\sin \theta_s$, the instrument's maximum OPD can be determined:

$$\delta_{\max} = \frac{y_{\max} \Delta S}{F}. \quad (3)$$

2.3 Sampling the Interferogram

The maximum OPD defines the spectral resolving capability of the instrument [12]. The most efficient way to improve the resolution is to increase the beam shear distance, ΔS . However, as δ_{\max} increases, care must be taken to avoid aliasing. Aliasing is avoided if the modulated waveform generated by the lens is sampled at a frequency greater than or equal to twice the bandwidth of the waveform. This is the Nyquist sampling criterion as paraphrased from Woodward [13]. It implies that a spectrum limited to a bandwidth of $\nu_{\max} - \nu_{\min}$ can be reconstructed perfectly if the interferogram is sampled uniformly at a frequency of N_s/δ_{\max} with at least the following number of sample points:

$$N_s \geq 2\delta_{\max}(\nu_{\max} - \nu_{\min}). \quad (4)$$

There is special significance associated with the value of δ_{\max} , which can be made clearer by setting $\nu_{\min} = 0$. If the number of samples for perfect reconstruction is $N_s = 2\delta_{\max}\nu_{\max}$, then in the spectral domain the sampling interval is $\Delta\nu_s = \nu_{\max}/N_s$ because the bandwidth is ν_{\max} . The Nyquist sampling criterion states that the bandwidth for perfect reconstruction increases with increasing N_s , which implies that $\Delta\nu_s$ must remain constant. Therefore, if the length of the interferogram is $\delta_{\max} - \delta_0$, and if δ_0 is zero, then the sampling interval must be fixed at

$$\Delta\nu_s = \frac{1}{2\delta_{\max}}. \quad (5)$$

This seems counter-intuitive, but the sampling interval³ in the spectral domain is fixed by the length of the interferogram and not by the number of samples or the spectral bandwidth. Increasing the number of interferogram samples only increases the possible spectral bandwidth that can be unambiguously reconstructed. If the number of pixels available to sample the interferogram is less than ν_{\max}/N_s , then the spectrum must be folded at some integer number of the Nyquist folding frequency:

$$\nu_N = m\Delta\nu_s N_s, \quad m = 1, 2, 3 \dots \quad (6)$$

If the interferogram has minimal sampling, then the spectral bandwidth must be limited by the optical or detector passband to avoid aliasing. The QWIP is ideal because it naturally limits the spectral passband to within the Nyquist folding order, which relaxes the filtering requirements.

³The spectral sampling interval is not equal to the spectral resolution, which can be defined arbitrarily. Griffiths [12] has determined that the spectral resolution by Rayleigh's criterion is $0.73/\delta_{\max}$.

2.4 The Pixel Width Attenuation Factor

The highest frequency at which the spectrum can be Nyquist folded is the point where the modulation period of the shortest wavelength equals the active width of the pixel, d_a (the pixel pitch minus the dead zone width). At this point the modulation efficiency of that wavelength goes to zero. A pixel width attenuation factor can be determined from equation 3 by defining the active width sampling function as

$$\Delta\delta_a = \frac{d_a \Delta S}{F}, \quad (7)$$

and then normalizing its Fourier transform into a $\sin x / x$ function:

$$\eta_v(d_a, \nu) = \frac{1}{\Delta\delta_a} \int_{-0.5\Delta\delta_a}^{0.5\Delta\delta_a} \exp(-i2\pi\delta\nu) d\delta = \left| \text{sinc} \left(\pi\nu \frac{d_a \Delta S}{F} \right) \right|. \quad (8)$$

Equation 8 is plotted in figure 5 and shows how the modulation efficiency improves if the width of the pixels decrease from $25 \mu\text{m}$ to $16 \mu\text{m}$. If it is not possible to produce a detector array with sufficiently small pixels, then the best option is to increase $\Delta\nu_s$. For example, if the pixel width is fixed at $25 \mu\text{m}$, then the spectral interval must be increased from 1 cm^{-1} in the 512 pixel case to 4 cm^{-1} in the 320 pixel case to eliminate the null point. The other option is to heterodyne the spectrum using a moiré filter. The moiré filter is a pattern of alternating transmitting and reflecting (or absorbing) bars. It resembles a transmission grating and is placed immediately above the detector array to block the destructive high-frequency modulations. The frequency of the bars is set at the lowest frequency of the spectrum in order to translate the spectrum to the zero wavenumber bin. There is a 50 % loss in energy across the entire spectral band, but the null points are eliminated from the spectrum.

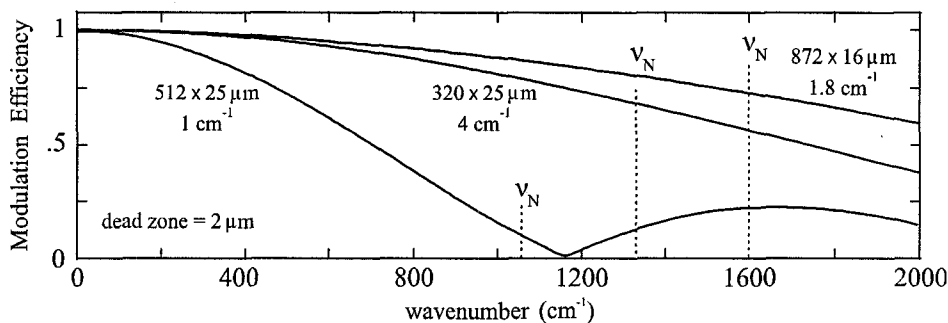


Figure 5: The modulation efficiency increases if either the width of the pixels decrease or $\Delta\nu_s$ increases.

2.5 Generating a Spectrum

If the pixel number, pixel width and spectral bin width are specified correctly, then it is possible to transform the modulation pattern unambiguously into a spectrum. First the detector array records the interferogram as voltages, and then the voltages are converted into digital numbers using analog to digital converters (ADCs). The next step is to process the data with a digital signal processor (DSP). This involves baselining the interferogram, performing a phase correction using either the Mertz or Foreman method [12], and then transforming the corrected interferogram into a spectrum using a Fast Fourier Transform (FFT). As shown in figure 6, each interferogram represents one instantaneous field-of-view (IFOV) of the image, and each of these interferograms is transformed separately into a spectrum. The transmission profiles are generated by taking a ratio between the spectrum and the estimated black body emission from the planet's surface. In this particular case the planet is Earth and a volcanic eruption is being detected in the first IFOV. Because the interferogram automatically separates the broadband ground emission from the narrowband vapor features, the SO_2 could have been detected in the interferogram domain by using the interferogram as a matched filter. This approach would enable the automated detection of volcanic plumes [14], which would be of significant benefit to commercial aircraft flying near active volcanoes [15]. The static interferometer is particularly suited for this task because the interferogram is sampled identically during every data collection period, which would not be the case in a scanning Michelson interferometer. Another application involves the detection of chemical agents from an Unmanned Airborne Vehicle (UAV). The matched filter approach reduces the on-board processing requirements and enables a detection to be made in real-time.

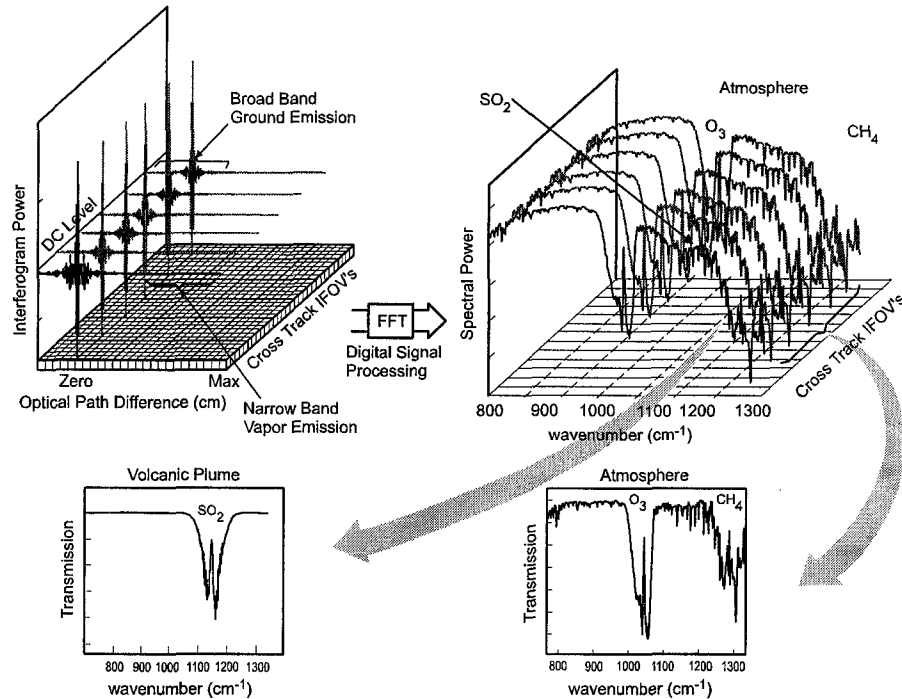


Figure 6: The transformation of digitized interferograms of the Earth's atmosphere into spectral profiles. The atmosphere and volcanic plume were simulated by Vince Realmuto of the Jet Propulsion Laboratory.

2.6 The Beam-Shearing Prism

There are many types of interferometer configurations that can be used to generate a spatially modulated interference pattern, the difficulty is in finding a compact configuration that will maximize the SNR while generating a single instrument line shape (ILS) for the entire image and spectrum. One compact design form is the recently invented beam-shearing prism [16] shown in figure 7. It consists of 3 separate potassium bromide prisms hard mounted in an aluminum structure. The first prism has a mirror coating on half of its front surface and a germanium beam-splitter coating on half of its back surface. The beam-splitter surface is tilted at less than 10° to avoid total-internal-reflection (TIR) at the air gap between the first and second prisms. Without this design feature the beam-splitter would have to be immersed in oil to avoid TIR. This is not a desirable option in a flight instrument because of possible evaporation and leakage problems. Another desirable feature of the prism triplet is the orientation of the entrance and exit surfaces, which are perpendicular to the diverging entrance and exit beams. This eliminates astigmatism, which severely degrades the spectral resolution in a spatially modulated interferometer [17]. The design shown in the figure is the size of a human thumb and is capable of generating a 25 mm beam shear in a 1 cm^{-1} interferometer. This represents a factor of 40 reduction in volume with respect to the less efficient Michelson, Sagnac, and Wollaston prism interferometers, which can only deliver half the input beam to the detector. The beam-shearing prism can deliver the entire beam to the same detector array, which improves the SNR of the instrument by a factor of 2 when it is background, dark current, or read noise limited.

In figure 8 a comparison is made between the optical efficiency of the beam-shearing prism, the Michelson interferometer, and a 1st order concentric, convex grating spectrometer [18]. The interferometers have the clear advantage in terms of broadband spectral coverage. In the narrow-band case the prism maintains its advantage over the grating. The advantage is increased significantly for applications that require very high throughput and relatively high spectral resolution—such as detecting minute amounts of poisonous chemical agents from a low altitude UAV. This throughput advantage is clearly shown in the right-hand plot where the slit is widened to allow a 5 mrad, $F/3$ beam of light to pass through. The design assumes a telescope with a 100 mm focal length and a spectrometer with two 20 mm detector arrays with $20 \mu\text{m}$ pitch. The grating spectrometer is hampered because its spectral resolution is directly proportional to the width of the entrance slit. If the slit is widened then either the length of the spectrum must be increased

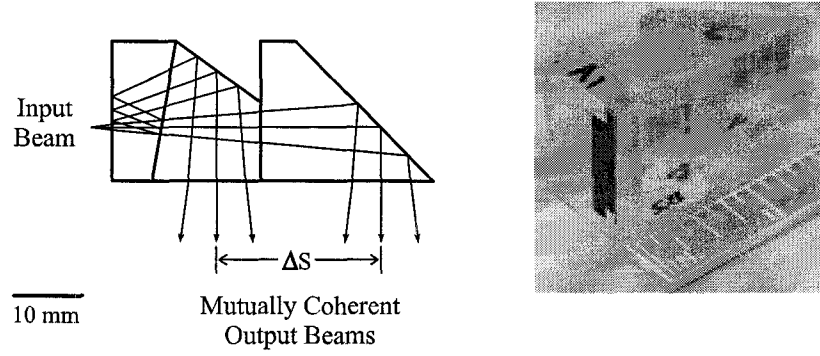


Figure 7: The beam-shearing prism enables the detector array to utilize 100 % of the input beam to maximize the SNR. This design generates a 25 mm beam shear for a 1 cm^{-1} interferometer. The coated prisms shown on the right were supplied by Pete Brendal Associates.

proportionately, or the spectrometer must be designed with a significant magnification. Unfortunately the convex grating spectrometer must operate near unity magnification, and it is the only known design form capable of maintaining low distortion over an appreciable field and spectrum [19]. Increasing the dispersion is not an option because distortion increases as the cube of the length of the spectrum. Despite the distortion problem, the spectral resolution of the grating (30 cm^{-1} at $5 \mu\text{m}$) is insufficient to resolve fine atmospheric features.

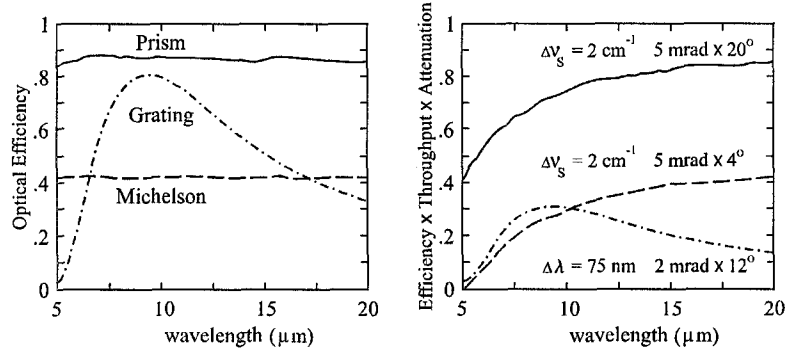


Figure 8: The efficiency of the prism interferometer is compared to a grating spectrometer and a Michelson interferometer. The right-hand plot shows the degradation in efficiency caused by pixel width attenuation in the prism interferometer, self apodization in the Michelson interferometer, and loss of throughput from the slit in the grating spectrometer. The grating resolution is $\Delta\lambda = 75 \text{ nm}$, or 30 cm^{-1} at $5 \mu\text{m}$.

The Michelson is not a field-widened interferometer, so its modulation efficiency suffers from self apodization as the slit is widened [12]. In this design comparison, self apodization limits the maximum extent of the field-of-view (FOV) to only 4° . The prism interferometer is not limited in its FOV, though it does suffer from the pixel width attenuation problem mentioned in section 2.4. The FOV in this particular design can easily be magnified to 20° in the direction parallel to the slit without having any impact on the pixel width attenuation factor. In the direction orthogonal to the slit the prism interferometer is field-widened because its detector is positioned at a pupil plane. All field angles converge at the same point in each zone of the pupil, no matter how wide the field is increased. Operating at a pupil plane also eliminates the diffraction Airy disc pattern, which enables the pixels to be reduced to any width for any wavelength without affecting the spectral resolution or ILS function. This is a significant advantage for atmospheric retrievals because the forward model of the atmosphere does not have to be adjusted at each wavelength to accommodate a changing ILS. The ILS changes for different field positions in the Michelson and for different wavelengths in the grating spectrometer.

2.7 Instrument Configurations

The spatially modulated interferometer can cover a 2 - 50 μm spectral bandwidth using a single cesium iodide beam-splitter if the Fourier optics and the telescope are designed entirely with mirrors. The difficulty is that an off-axis Fourier optical system must be made anamorphic to generate an image perpendicular to the interferogram pupil plane. Such a design is shown in figure 9. It consists of four off-axis aspheres, three of which are anamorphic. The mirrors were diamond turned by Symons under subcontract to the physics department at the University of Reading, who manufactured the mirror blanks and interferometer housing. Symons have built a special R- θ (radius-angle) diamond turning machine that achieves a much better surface quality than the traditional X-Y machines. This eliminates the need for post polishing the aspheres, which is costly and time consuming. The telescope, manufactured by the same two groups, is unique in that it has a shifted entrance pupil. Shifting the entrance pupil moves the chief ray to one edge of the exit pupil, which moves the zero OPD position, δ_0 , to one side of the detector array. This enables the Fourier optics to generate single-sided interferograms, as shown in figure 6. Using single-sided interferograms effectively doubles δ_{max} for the same detector and pupil widths.

Both the telescope and the Fourier optical system were designed to be telecentric in the plane of the interferograms. This is a requirement because collimated beams can only be made to converge at a pupil plane if both the telescope and the interferometer are telecentric. However, the Fourier optics is not telecentric in the image plane so that it can operate at unity magnification with respect to the entrance slit. This maximizes the spatial resolution, a requirement for the Mars application for detecting small vapor plumes with a spatial extent of approximately 200 - 300 meters. A much simpler design would use standard optics to generate the collimated beam and a cylindrical mirror to generate an image orthogonal to the interferogram plane. The cylindrical mirror design would reduce the focal length and spatial resolution considerably. Such a design would be acceptable for the application of sounding the Earth's atmosphere with a point spectrometer. The cylindrical mirror could have an extremely short focal length to compress the beam onto a line detector array to increase the SNR. An anamorphic refractive system made from germanium is the best solution for the application of detecting chemical agents from a low flying UAV. A low power cylindrical imaging lens can be used to augment an anamorphic Fourier lens to help magnify the field angles. Unlike the cylindrical mirror, which can have extremely high power, the cylindrical lens must be very low power, otherwise its thick center will shift the rays with respect to the rays traversing its thinner edges. This would generate a curved exit pupil and distort the interferogram.

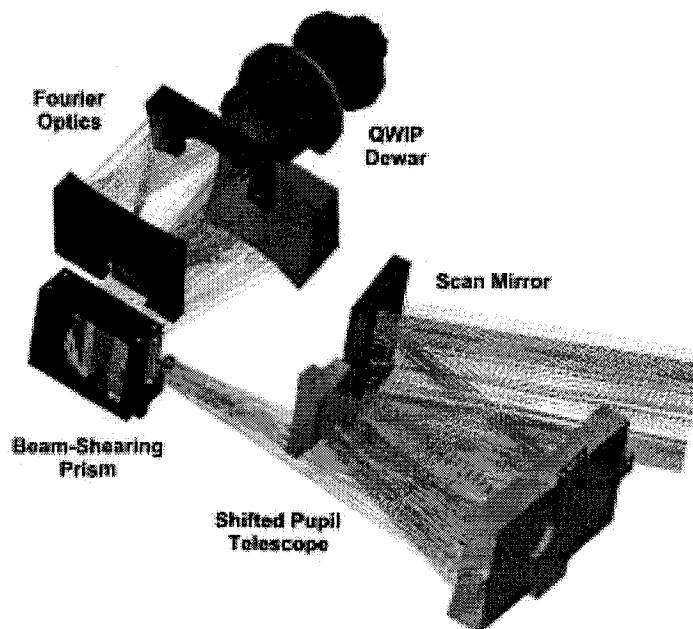


Figure 9: Spatially Modulated Prism Interferometer designed for $\Delta\nu_s = 1 \text{ cm}^{-1}$ and IFOV = 750 $\mu\text{radians}$.

The design shown in figure 9 is the prototype for the Mars water vapor detection experiment, though it would most likely be redesigned to operate at $\Delta\nu_s = 1.8 \text{ cm}^{-1}$ to minimize the pixel width attenuation at the shorter wavelengths. The prototype is based on the spatially modulated interferometer models developed with the aid of the Sagnac interferometer breadboard shown in figure 10. The Sagnac is useful because the beam shear distance, ΔS , can be varied by translating the offset mirror. The fundamental principles of spatially modulated interferometry are otherwise identical in both types of interferometers. The Sagnac has roughly the same throughput efficiency and volume as the Michelson, which would be too large in a high resolution design for a Mars micro-mission or a small UAV. Adjacent to the photograph is a plot of the first spectrum observed with the breadboard: the absorption of pure N_2O in a 5 cm long gas cell. The interferogram was recorded by a 488×640 narrow-band QWIP array [20] with a peak responsivity of 124 mA/W at $8.3 \text{ }\mu\text{m}$ when biased at -2 volts. The recorded spectrum was compared to several different simulations of N_2O . The simulation at $\Delta\nu_s = 4 \text{ cm}^{-1}$ for an ambient temperature of $290 \text{ }^\circ\text{K}$ and a cell pressure of 1 atmosphere seemed to match rather closely with the measured spectrum, though the ambient conditions were not controlled well enough to guarantee that they were identical to what was assumed for the simulation.

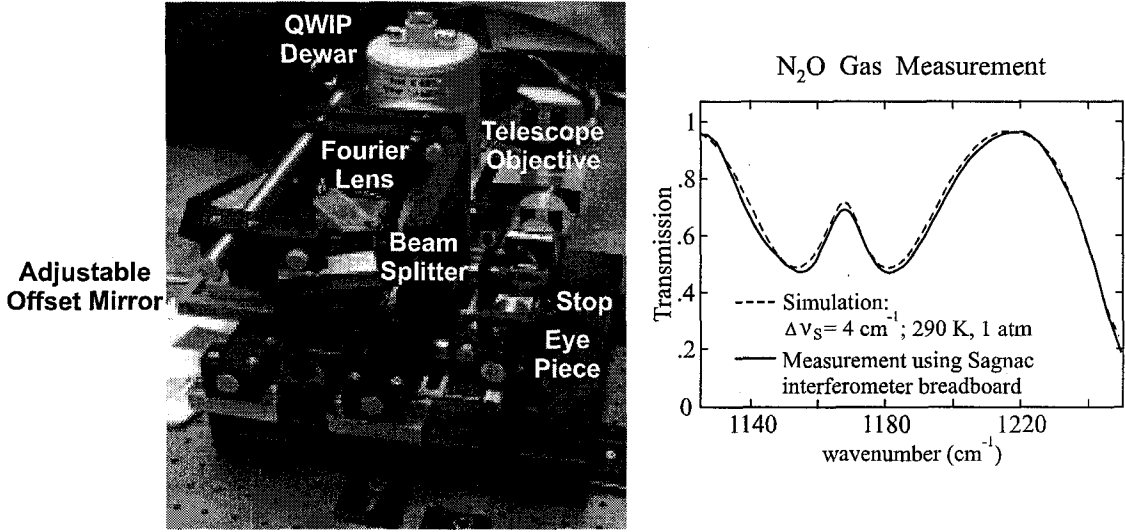


Figure 10: Sagnac interferometer breadboard and plot of first vapor measurement.

3 Dead Pixels

An uncorrected dead (or hot pixel) is the Achilles' heel of a spatially modulated interferometer. Its devastating effect on the spectrum can be determined by analyzing the process of Fourier transforming the interferogram. If $B_e(\nu)$ is the amplitude of the broadband source spectrum in units of electrons per wavenumber, and $A(\frac{\delta}{W})$ is the apodization or window function truncating or modifying the interferogram, then the interferogram amplitude recorded by an array of N_p pixels is

$$I_e(\delta) = A\left(\frac{\delta}{W}\right) \int_{\nu_{\min}}^{\nu_{\max}} \frac{B_e(\nu)}{N_p \Delta\delta} [1 + \cos(2\pi\nu\delta)] d\nu, \quad [e^-] \quad (9)$$

with

$$\Delta\delta = \frac{W}{N_p}, \quad (10)$$

and

$$W = \begin{cases} \delta_{\max} + \delta_\phi & \text{in a single-sided interferogram} \\ 2\delta_{\max} & \text{in a double-sided interferogram.} \end{cases}$$

The value δ_ϕ represents the maximum optical path difference on the negative side of δ_0 , the side used for phase correction in a single-sided interferogram. After subtracting the 'dc' term, the spectrum is determined

from the Fourier transform of equation 9:

$$S_e(\nu) = B_e(\nu) \otimes \int_{\nu_{\min}}^{\nu_{\max}} \frac{\mathcal{A}(\nu'W)}{2} [\delta_{\text{Dirac}}(\nu + \nu') + \delta_{\text{Dirac}}(\nu - \nu')] d\nu', \quad [\text{e}^-] \quad (11a)$$

$$= B_e(\nu) \otimes \frac{\mathcal{A}(\nu W)}{2}. \quad [\text{e}^-] \quad (11b)$$

The δ_{Dirac} terms represent shifted Dirac delta functions that are mirror images of each other. The negative frequency term is usually discarded because it contains no additional information. $\mathcal{A}(\nu W)$ is the Fourier transform of the window function and is called the spectral apparatus function. When $\mathcal{A}(\frac{\delta}{W})$ is a rectangle function (no apodization), then the $\otimes \frac{\mathcal{A}(\nu W)}{2}$ factor can be approximated by $\Delta\nu_s$.

A dead pixel is equivalent to multiplying the interferogram by an impulse, $\Delta B_d \delta_{\text{Dirac}}(\delta - \delta_d)$, where δ_d represents the relative interferogram position with respect to the zero path difference pixel, and ΔB_d represents the dimensionless relative difference between the actual voltage recorded at the pixel and the voltage that would have been recorded had the pixel been active. The Fourier transform of the altered interferogram yields the modified spectrum:

$$\mathcal{F}[\Delta B_d \delta_{\text{Dirac}}(\delta - \delta_d) I_e(\delta)] = \frac{\Delta B_d}{2} \cos(2\pi \nu \delta_d) \otimes B_e(\nu) \otimes \mathcal{A}(\nu W). \quad (12)$$

The effect of the dead pixel is to send a ripple through the spectrum, as shown in figure 11. On the left is a typical double-sided interferogram and its Fourier transformed spectrum. In the adjacent plot, pixel number 275 has no response. If pixel 275 remains uncorrected, then the Fourier transform of the interferogram will yield the erroneous spectrum shown below it.

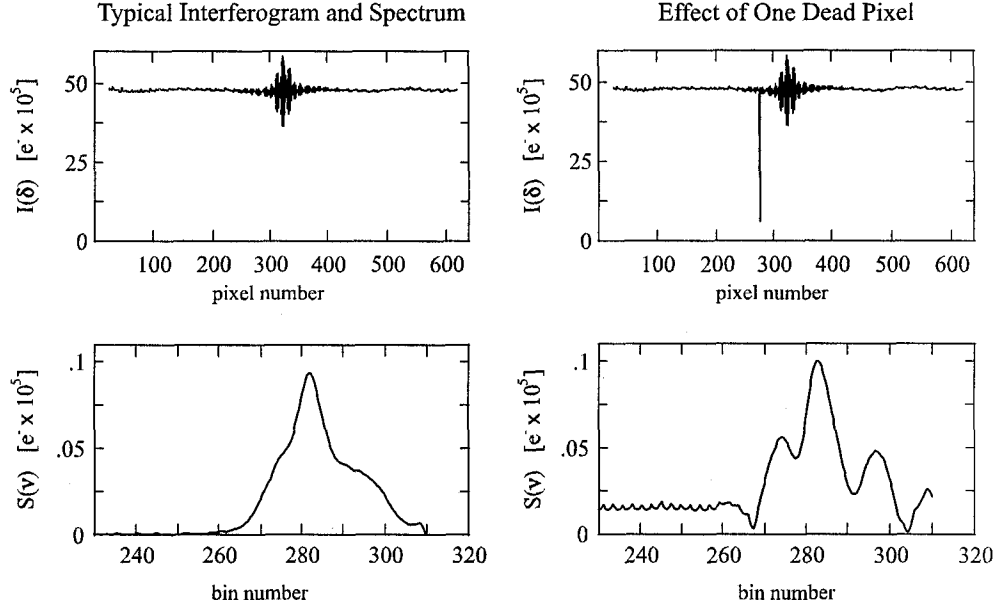


Figure 11: The effect on the spectrum of removing a single interferogram sample.

Fortunately the QWIP detector has a pixel operability greater than 99.9%, which is why it is the detector of choice for spatially modulated interferometers. If the number of dead pixels are reasonably small, then they can easily be corrected if the optics are designed to blur or defocus the image across a few interferogram rows. This allows the dead pixels to be replaced by active pixels in the same column because they would be illuminated by the same spatial scene. The bad pixels are tagged when the detector array is flat-field calibrated to set the digital gains and offsets. During data collection the tagged pixels are discarded, and the pixels that are vertically summed to form an interferogram sample are digitally weighted to account for the pixel loss. For example, if 4 pixels are needed to generate an interferogram sample, and one of the pixels is dead, then the remaining three pixels are multiplied by the factor 4/3. In a typical operational scenario, a dead pixel scan would be performed during every calibration period, which might occur every 10 to 20

minutes. A large gap between calibrations is acceptable when the QWIP detector is being used because its response does not change noticeably for at least an hour.

4 Pixel Response Nonuniformity Noise

Pixel response nonuniformity generates a multiplicative, fixed-pattern noise in any instrument that uses a detector array. However, in the spatially modulated interferometer this phenomenon is particularly pernicious because the noise is proportional to the integrated signal. This can have a devastating effect on the SNR in regions of the spectrum where the signal is weak. Fortunately the QWIP detector array has a very high uniformity, about 5.6 % when uncorrected, and about 0.03 % after a two-point flat-field calibration [21]. The required calibration accuracy can be determined by varying the response error until the SNR begins to decrease. This will be shown in section 6 using the noise model derived here.

An interferogram corrupted by fixed-pattern response noise can be modelled by multiplying the ideal broadband interferogram (equation 9) by a randomly varying, normalized pixel response function:

$$I_R(\delta) = \epsilon_R(\delta) A\left(\frac{\delta}{W}\right) \int_{\nu_{\min}}^{\nu_{\max}} \frac{B_e(\nu)}{N_p \Delta\delta} [1 + \cos(2\pi\nu\delta)] d\nu \quad [\text{e}^-] \quad (13)$$

where

$\epsilon_R(\delta)$ is the pixel response variation, a Gaussian random variable with a mean value of $\mu_R = 1$ and a standard deviation of σ_R .

The parameters $\epsilon_R(\delta)$, μ_R , and σ_R are defined as dimensionless quantities.

When the ‘dc’ term is subtracted during the baselining process, the statistics of the pixel response variation are not effected. However, the ‘dc’ noise remains and is imbedded in the ‘ac’ noise. The ‘ac’ noise is a deterministic random process that is neither ergodic or stationary. Its autocorrelation function does not reduce to a simple function of $\Delta\delta = \delta_{k+1} - \delta_k$, and strictly speaking, the Wiener-Khinchine relation cannot be used to determine the noise spectrum. However, Rayleigh’s conservation of power theorem (also known as Parseval’s theorem in connection with Fourier series) can be used:

$$\Delta\nu_s \sum_{m=0}^{2N_s-1} |S_R(m\Delta\nu_s)|^2 = \Delta\delta \sum_{k=0}^{N_p-1} |I_R(k\Delta\delta)|^2, \quad (14)$$

The power spectrum can be obtained from equation 14 by dividing through by $\Delta\nu_s N_s$ and transforming $\Delta\delta$ into $\Delta\nu_s$ using equations 5 and 10:

$$\Delta\delta = \frac{1}{2\Delta\nu_s N_s}, \quad (15)$$

with

$$N_s = N_p - N_\phi$$

and

$$N_\phi = \begin{cases} N_p/2 & \text{in a double-sided interferogram} \\ N_p \delta_\phi / W & \text{in a single-sided interferogram.} \end{cases}$$

After substituting equation 13 for I_R , the noise spectrum is determined from the ensemble average of the power spectrum:

$$\begin{aligned} \langle |S_R(\nu)|^2 \rangle &= \frac{1}{(2\Delta\nu_s N_s)^2} \sum_k \sum_l \left\langle \epsilon_R(k\Delta\delta) \epsilon_R(l\Delta\delta) A\left(\frac{\delta}{W}\right) A\left(\frac{\delta + \Delta\delta}{W}\right) \right\rangle \\ &\times \int_{\nu_{\min}}^{\nu_{\max}} \frac{B_e(\nu)}{N_p \Delta\delta} [1 + \cos(2\pi\nu k \Delta\delta)] d\nu \int_{\nu_{\min}}^{\nu_{\max}} \frac{B_e(\nu)}{N_p \Delta\delta} [1 + \cos(2\pi\nu l \Delta\delta)] d\nu \quad (16) \end{aligned}$$

The expectation operator is applied only to the apodized pixel response variation term because it is the only random variable in the equation. The response variation is a stationary process with Gaussian statistics, so the expected value of its autocorrelation function is the variance, σ_R^2 , when $k = l$. The noise samples

are uncorrelated, so the autocorrelation function rapidly approaches zero when $k \neq l$. This enables the two summations to be combined into one again, and the resulting summation of each cosine integral reduces to $\frac{1}{2}$ for large N_p . Assuming no phase correction is made to the interferogram, the rms pixel response noise is

$$\sigma_{Re} = \frac{\sigma_R A_{rms}}{2 \Delta \nu_s N_s} \sqrt{N_p} \int_{\nu_{min}}^{\nu_{max}} B_e(\nu) d\nu, \quad [\text{rms e-}] \quad (17)$$

with the rms apodization function defined as

$$A_{rms} = \sqrt{\frac{1}{W} \int_{-\frac{W}{2}}^{\frac{W}{2}} A^2\left(\frac{\delta}{W}\right) d\delta}. \quad [\text{cm}^{-1}] \quad (18)$$

When $A\left(\frac{\delta}{W}\right)$ is a rectangle function (no apodization), then A_{rms} is approximately equal to $\Delta \nu_s$. If a phase correction is applied to the interferogram before the Fourier transformation process, then the imaginary part of the spectrum can be discarded, and with it half the noise. Therefore equation 17 can be divided by $\sqrt{2}$ for the phase corrected case.

It is clear that pixel response noise is multiplicative because the response variation is multiplied by the integral of the source spectrum. It is also apparent that as $N_p \rightarrow N_s$ (the single-sided interferogram case), the noise decreases in proportion to the square root of the number of pixels. The same effect is true of the double-sided interferogram, though it has $\sqrt{2}$ more noise because it has twice as many pixels for the same number of spectral samples. The noise reduction effect of increasing the number of pixels is shown clearly in figure 12, which is a simulation of equation 13 using a random pixel response error of 1 %. If the number of pixels is increased from 320 to 1000 and the value of $\Delta \nu_s$ is held constant by proportionately reducing the pixel width, then the Nyquist folding frequency, ν_N , is increased in direct proportion to the number of pixels. The resulting spectral noise is distributed over a broader spectral bandwidth, which effectively reduces its contribution to the SNR. Conversely, if the number of pixels is reduced, then the noise is aliased back into the spectrum. Notice that the difference between the noisy interferogram and the ideal interferogram, $I_R(\delta) - I(\delta)$, is uniform white noise. Likewise, in the spectral domain the noise has no spectral content—it is uniformly distributed across the spectrum.

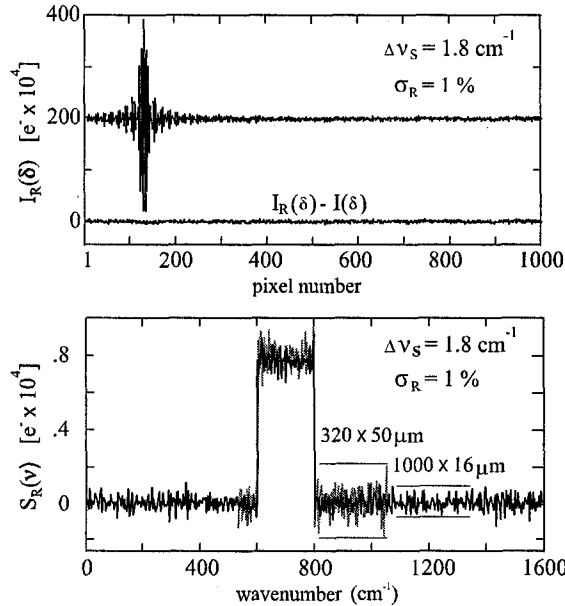


Figure 12: Pixel response nonuniformity noise for $N_p = 320$ pixels and 1000 pixels.

5 Pixel Position Error Noise

Pixel position errors in detector arrays are set by the overlay and stitching accuracies of the machine that manufactures the detector mask sets. The QWIP masks designed at the Jet Propulsion Laboratory (JPL) are fabricated by Paul Maker using an electron beam with a 3σ overlay accuracy of 50 nm within a 600 μm field. Each of the 600 μm fields can be stitched together with a 3σ accuracy of 70 nm. The stitching and overlay accuracies have no effect on the 'dc' signal level or noise, but they do affect the sampling of the interferogram. The sampling errors can be modelled in the interferogram as random variations in optical path difference:

$$I_P(\delta) = A \left(\frac{\delta}{W} \right) \int_{\nu_{\min}}^{\nu_{\max}} \frac{B_e(\nu)}{N_p \Delta\delta} \cos \{2\pi\nu[\delta + \epsilon_P(\delta)]\} d\nu \quad (19a)$$

$$= I_{ac}[\delta + \epsilon_P(\delta)], \quad (19b)$$

where

$$I_{ac}(\delta) = A \left(\frac{\delta}{W} \right) \int_{\nu_{\min}}^{\nu_{\max}} \frac{B_e(\nu)}{N_p \Delta\delta} \cos(2\pi\nu\delta) d\nu, \quad (20)$$

and

$\epsilon_P(\delta)$ is the pixel position error, a Gaussian random variable with a mean value of $\mu_P = 0$ and a standard deviation of σ_P .

The parameters $\epsilon_P(\delta)$ and σ_P are defined in units of optical path difference.

It would be difficult to evaluate the noise with the random variable imbedded in the cosine function. For Michelson interferometers, Sanderson [22] suggests approximating the sample error effect with a Taylor series expansion of the interferogram. Sanderson's approach is valid if the errors are small compared to the period of the interferogram fringes, which is the case in a spatially modulated interferometer. It is therefore possible to use the increment form of the Taylor series to expand equation 19b:

$$I_P(\delta) \simeq I_{ac}(\delta) + \epsilon_P(\delta) \frac{d}{d\delta} [I_{ac}(\delta)] \quad \text{for } \epsilon_P(\delta) \ll \Delta\delta. \quad (21)$$

When evaluating this equation for noise, the first term can be ignored because the random variable has been isolated to the second term. The noise is clearly multiplicative because it is directly proportional to the signal amplitude through the derivative term.

Two derivations of the spectral noise will be presented. In the first derivation, the derivative is taken of equation 20 and multiplied by the random error to provide the differential interferogram error:

$$I_{dP}(k\Delta\delta) = \epsilon_P(k\Delta\delta) \frac{d}{d\delta} [I_{ac}(\delta)] \quad (22a)$$

$$= -\epsilon_P(k\Delta\delta) A \left(\frac{k\Delta\delta}{W} \right) 2\pi \int_{\nu_{\min}}^{\nu_{\max}} \frac{\nu B_e(\nu)}{N_p \Delta\delta} \sin(2\pi\nu\delta) d\nu. \quad (22b)$$

Using the steps outlined in section 4, the power spectrum of the interferogram is determined from Rayleigh's theorem— equation 14 with $I_R(k\Delta\delta)$ replaced by $I_{dP}(k\Delta\delta)$. The position error, like the pixel response error, is a stationary, Gaussian random variable with an autocorrelation function equal to its variance, σ_P^2 . After making the appropriate substitutions, the rms noise reduces to

$$\sigma_{P\epsilon} = \frac{\pi \sigma_P A_{\text{rms}}}{\Delta\nu_s N_s} \sqrt{\sum_k^{N_p} \left[\int_{\nu_{\min}}^{\nu_{\max}} \nu B_e(\nu) \sin(2\pi\nu k\Delta\delta) d\nu \right]^2} \quad [\text{rms e-}] \quad (23)$$

In the second derivation Rayleigh's theorem is again invoked to indicate the conservation of noise power in both transform domains:

$$\langle |S_{dP}(\nu)|^2 \rangle = \frac{\Delta\delta}{2\Delta\nu_s N_s} \sum_k^{N_p} \sum_l^{N_p} \langle \epsilon_P(k\Delta\delta) \epsilon_P(l\Delta\delta) \rangle \left| \frac{d}{d\delta} [I_{ac}(\delta)] \right|^2 \quad (24)$$

$$= \begin{cases} \frac{\sigma_P^2}{2\Delta\nu_s N_s} \Delta\delta \sum_k^{N_p} \left| \frac{d}{d\delta} [I_{ac}(\delta)] \right|^2, & k = l \\ 0, & k \neq l \end{cases} \quad (25)$$

However, at this point equation 22b is not substituted for the differential interferogram. Instead, the derivative form of the Fourier transform is used together with Rayleigh's theorem to express the derivative of the measured spectrum, $S_e(\nu)$:

$$\langle |S_{dP}(\nu)|^2 \rangle = \frac{\sigma_P^2}{2\Delta\nu_s N_s} \Delta\nu_s \sum_m^{2N_s} |2\pi m \Delta\nu_s S_e(m \Delta\nu_s)|^2. \quad (26)$$

It is now possible to use equation 11b to redefine the measured spectrum in terms of the input spectrum, $B_e(\nu)$. The measured spectrum is equal to half of the input spectrum convolved with the apparatus function $A(\nu W)$:

$$\langle |S_{dP}(\nu)|^2 \rangle = \frac{(2\pi\sigma_P)^2}{2\Delta\nu_s N_s} \Delta\nu_s \sum_m^{2N_s} \left| m \Delta\nu_s \frac{1}{2} A(m \Delta\nu_s W) \otimes B_e(m \Delta\nu_s) \right|^2 \quad (27)$$

$$= \frac{(\pi\sigma_P)^2}{2\Delta\nu_s N_s} \int_{\nu_{\min}}^{\nu_{\max}} [\nu A(\nu W) \otimes B_e(\nu)]^2 d\nu. \quad (28)$$

For consistency with the other noise equations, the apparatus function will be converted into its rms apodization form, A_{rms} , by integrating across the ILS function. It would also be more appropriate to convert the position error, σ_P , into the dimensions of the detector array rather than the optical path difference. Therefore the rms pixel position error becomes

$$\sigma_{P\epsilon} = \pi \hat{\sigma}_P A_{\text{rms}} \sqrt{\frac{\int_{\nu_{\min}}^{\nu_{\max}} [\nu B_e(\nu)]^2 d\nu}{2\Delta\nu_s N_s}}, \quad [\text{rms c-}] \quad (29)$$

with

$$\hat{\sigma}_P = \sigma_P \frac{y_{\max}}{\delta_{\max}}. \quad [\mu\text{m}] \quad (30)$$

Simulations have shown that with σ_P converted into $\hat{\sigma}_P$, equation 23 is exactly equivalent to equation 29, though it is much quicker and easier to evaluate the latter. In both cases the noise can be divided by $\sqrt{2}$ to account for phase correction.

In figure 13 are shown simulations of an interferogram and spectrum with a very large position error: $\hat{\sigma}_P = 1 \mu\text{m}$. In the upper plot an ideal interferogram is subtracted from the noisy interferogram to reveal a significant amount of noise around δ_0 , where the amplitude oscillations are greatest. However, in the spectral domain the noise appears to be rather evenly distributed inside and outside of the spectral signal band. Once again, if the number of pixels are reduced from 1000 to 320, then the noise increases significantly.

6 Signal to Noise Ratio

In this section the SNR will be computed for a future Mars micro-mission to map water vapor sources. In table 1 are listed the spacecraft orbital parameters and the instrument design parameters. The spacecraft will be put in an elliptical orbit to conserve fuel during orbit insertion. To conserve power the instrument will only be switched on when it approaches the perigee phase of each orbit. During the telemetry (apogee) phase of each orbit, the detector temperature will be allowed to rise to approximately 180° K. The orbital inclination will be set at 30° to concentrate the mapping measurements along possible future sample-return landing sites, which must be located within a $\pm 30^\circ$ latitude band to enable the samples to be easily launched back into orbit for the rendezvous with the return spacecraft. At the perigee altitude of 380 km the projected footprint will be 307 meters long and moving at 4 km/sec.

The detector dark current noise, the thermal background noise, the signal shot noise, the readout noise, and the digitization noise can all be derived using the procedures outlined in the previous two sections. All of the noise sources remain uncorrelated if a digital apodization window is not applied to the interferogram. They can therefore be root-sum-squared to form the total noise contribution in the SNR calculation. The SNR is computed using the listed design parameters for a given set of atmospheric and surface conditions. It is anticipated that the surface temperature will be 270° K at 12 noon near the equator under nominal

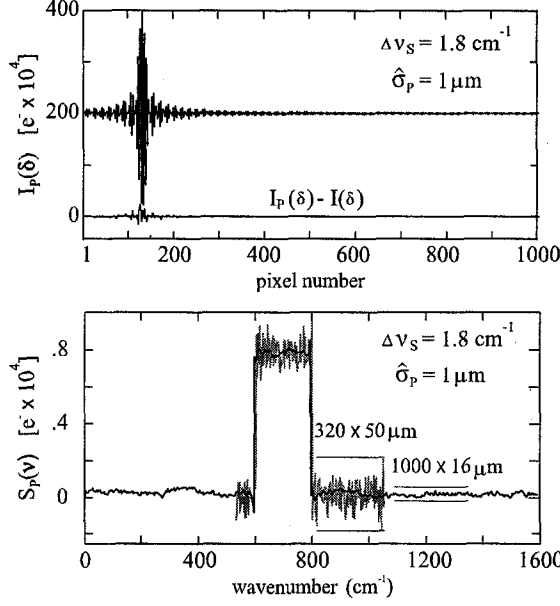


Figure 13: The position error increases the interferogram noise near pixel 128 ($\delta = \delta_0$). The spectral noise is evenly distributed and significantly reduced when the number of pixels is increased from 320 to 1000.

Spacecraft	i 30°	e 0.7	L_{FP} 307 meters	H_P 380 km	V_{FP} 4 km/s	T_{Mars} 270° K
Telescope	Pupil 50 × 40 mm	F_t 200 mm	$IFOV$ 790 μ rad	FOV 65 mrad	T_{exp} 77 msec	T 290° K
Interferometer	N_s 872	$\Delta\nu_s$ 1.835 cm ⁻¹	y_{max} 13.95 mm	ΔS 12.5 mm	F 64 mm	T 180° K
QWIP	N_p 1000	pitch 16 μ m	I_{dark} 0.01 & 340 pA	QE_{peak} 0.5 & 0.067	G_ν 0.29	T 45° K

Table 1: Flight Instrument Design Parameters.

dust conditions: $I_{ROD} = 0.05$. The average surface emissivity is expected to be 0.95. The instrument will be a lower resolution version of the all-reflective design shown in figure 9. The QWIP detector will be a dual broadband array with the normalized responsivity shown in figure 3 and an operating bias of -2.5 volts. The dark current of the LWIR pixels have been measured at $I_{dark} = 340$ pA, and the peak quantum efficiency has been measured at $QE_{peak} = 0.067$. It is hoped that the quantum efficiency for the MWIR pixels can be increased to 0.50. There will be negligible dark current for the MWIR pixels because the cut-off wavelength will be short and the temperature will be lower than necessary.

In figure 14 is plotted the SNR as a function of pixel response error and pixel position error at four different wavelengths. The other noise sources are held constant. The longer wavelengths are limited by dark current noise, and the shorter wavelengths are limited by background noise and read noise (assumed to be 500 rms electrons). It is apparent that the break point at which the response noise begins to dominate is $\sigma_P = 0.05\%$ at the shorter wavelengths. The typical QWIP two-point calibrated response error is 0.03%, which is within the requirement. The more likely error is only 0.01%. The break point for the position error is $\hat{\sigma}_P = 20$ nm, which is exactly the limit of the current QWIP fabrication technology. By the time the flight focal plane will be ready for fabrication, the technology will have reduced the stitching and overlay errors to $\hat{\sigma}_P = 5$ nm, which provides considerable margin. It is fair to state that the interferometer should not suffer from multiplicative noise.

The water vapor band extends from 6.5 to 7.5 μ m. As shown in the two plots, when the multiplicative noises are reduced to an acceptable level, then the SNR in the water band ranges from 200 to 800. This is sufficient to enable detection of water vapor to an accuracy of 1 μ m between 10 am and 4 pm under nominal dust conditions. However, the QWIP design assumes a 1000 pixel array with 16 μ m pitch. Such an array

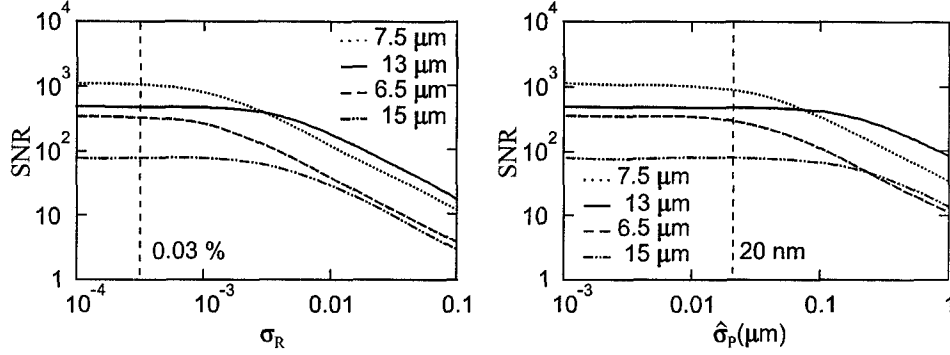


Figure 14: SNR vs pixel response error and pixel position error at 4 wavelengths for the Mars micro-mission at 12 noon with nominal dust. Dashed vertical lines show limits of current QWIP technology.

has never been manufactured. It is therefore important to understand how the pixel number and pixel pitch influence the SNR. In figure 15 the SNR is plotted against the number of pixels assuming a constant sample width of $\Delta\nu_s = 1.835 \text{ cm}^{-1}$. The pixel pitch is scaled inversely with the number of pixels to keep the array size constant. The SNR increases with pixel number for all wavelengths, but the improvement is the most dramatic when the signal level is high. The SNR in the water band is still sufficient at the 640 pixel mark, but a 1000 pixel array would offer a significant improvement.

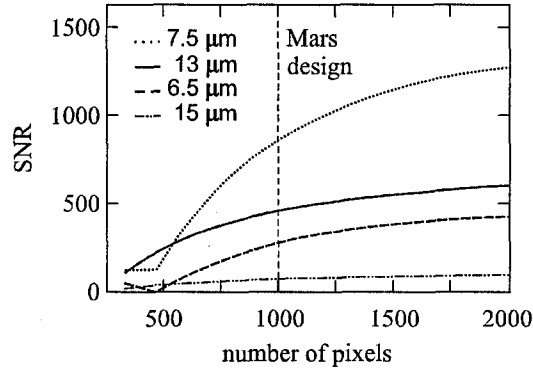


Figure 15: SNR vs number of detector pixels for the Mars micro-mission at 12 noon with nominal dust.

7 Conclusions

The detection of water vapor sources in a dusty atmosphere requires an instrument with a sampling interval smaller than 2 cm^{-1} , a spatial resolution of 300 meters, and a SNR greater than 100 from 6.5 to 7.5 μm and from 14 to 15.5 μm . The Spatially Modulated Prism Interferometer is capable of achieving these requirements if the detector array has a minimum of 640 pixels with a pixel response error of less than 0.05 % and a pixel position error of less than 20 nm. The pixel response and pixel position error requirements are within the limits of current QWIP technology. Significant improvements can be made in the SNR if the number of pixels are increased from 640 to 1000. This reduces the pixel width attenuation at the shorter wavelengths, and it reduces the noise throughout the spectrum. The high operability of the QWIP array minimizes the possibility that a dead pixel, or clusters of dead pixels, will corrupt the spectrum.

The current instrument configuration would weigh approximately 10 kg. This fits within the constraints of the current micro-spacecraft technology. A 3 kg version of the instrument is under development using germanium lenses and a smaller telescope. The germanium limits the spectral passband to a 6 - 15 μm bandwidth, which is suitable for detecting chemical agents from an UAV. The UAV mission requires very high efficiency, which is easily obtained by widening the slit. Because the interferogram is generated at a pupil plane, the slit width has no influence on the spectral resolution.

Acknowledgements

This work was supported by the Director's Research and Development Fund at the Jet Propulsion Laboratory and by the Technology Application Program office of the National Aeronautics and Space Administration. The author is grateful to Sumith Bandara, Michael Grimm, Sarath Gunapala, Dean Johnson, John Liu, and Don Rafol for their help in developing the instrument hardware and software, and to Ella Makarkina for her help in preparing the drawings. Hardware components for the SMPI were supplied by Indigo Systems, Pete Brendal Associates, Symons Mirror Technology, and the University of Reading's Department of Physics.

References

- [1] M. Carr, Water on Mars, Oxford University Press, 1996.
- [2] M. Malin and K. Edgett, *Science* **288**, 2330 (30 June 2000).
- [3] M. Sims, Hydrothermal vent on mars, 1998, Email correspondence from Leicester University to Fred Taylor of Oxford University.
- [4] D. McCleese, R. Haskins, J. Schofield, R. Zurek, and et. al., *Journal of Geophysical Research* **97**, 7735 (1992).
- [5] M. Born and E. Wolf, Principles of Optics, Pergamon Press, Oxford, 1970.
- [6] G. Stroke and A. Funkhouser, *Physics Letters* **16**, 272 (1965).
- [7] K. Yoshihara and A. Kitade, *Japanese Journal of Applied Physics* **6**, 116 (1967).
- [8] T. Okamoto, S. Kawata, and S. Minami, *Applied Optics* **23**, 269 (1984).
- [9] T. Barnes, *Applied Optics* **24**, 3702 (1985).
- [10] W. Smith, *Experimental Astronomy* **1**, 389 (1991).
- [11] J. Rafert, R. Sellar, and J. Blatt, *Applied Optics* **34**, 7228 (1995).
- [12] P. Griffiths and J. de Haseth, Fourier Transform Infrared Spectrometry, volume 83 of Chemical Analysis, John Wiley and Sons, 1986.
- [13] M. Woodward, Probablility and Information Theory, Pergamon Press, New York, 1955.
- [14] V. Realmuto, A. Sutton, and T. Elias, *Journal of Geophysical Research* **B7**, 102 (1997).
- [15] T. Casadevall, Volcanic ash and aviation safety: Proceedings of the first international symposium on volcanic ash and aviation safety (july 1991), in US Geological Survey Bulletin, page 2047, 1994.
- [16] F. Reininger, Spatially modulated interferometer and beam shearing device therefor, United States Patent Application, 2000.
- [17] F. Reininger, A Spatially Modulated Interferometer for mapping Martian water vapour sources, PhD thesis, University of Oxford, Department of Atmospheric Physics, 2000.
- [18] F. Reininger, A. Coradini, F. Capaccioni, and et. al., VIRTIS: Visible infrared thermal imaging spectrometer for the rosetta mission, in Imaging Spectrometry II, pages 66 – 77, SPIE, 1996, Volume 2819.
- [19] F. Reininger, Imaging Spectrometer/Camera having convex grating, United States Patent, 2000, Number 6100974.
- [20] S. Gunapala and et. al., *SPIE Proceedings* **3061**, 722 (1997).
- [21] S. Gunapala, S. Bandara, J. Liu, and et. al., *IEEE Transactions on Electron Devices* **47**, 326 (2000).
- [22] R. B. Sanderson, Fourier spectroscopy, in Molecular Spectroscopy: Modern Research, edited by K. N. Rao and C. W. Mathews, chapter 7, pages 297 – 325, Academic Press, 1972.